

# Comparison of simulation and experiments for multimode aerodynamic breakup of a liquid metal column in a shock-induced cross-flow

Cite as: Phys. Fluids **31**, 082110 (2019); <https://doi.org/10.1063/1.5099589>

Submitted: 11 April 2019 . Accepted: 26 July 2019 . Published Online: 16 August 2019

Marco Arienti , Matthew Ballard , Mark Sussman , Yi Chen Mazumdar , Justin L. Wagner, Paul A. Farias, and Daniel R. Guildenbecher 



[View Online](#)



[Export Citation](#)



[CrossMark](#)

## ARTICLES YOU MAY BE INTERESTED IN

[Saturated film boiling over a circular cylinder subjected to horizontal cross-flow in the mixed regime](#)

[Physics of Fluids](#) **31**, 082109 (2019); <https://doi.org/10.1063/1.5099075>

[Three-dimensional numerical simulation of bubble rising in viscous liquids: A conservative phase-field lattice-Boltzmann study](#)

[Physics of Fluids](#) **31**, 063106 (2019); <https://doi.org/10.1063/1.5096390>

[Modeling and verification of the Richtmyer–Meshkov instability linear growth rate of the dense gas-particle flow](#)

[Physics of Fluids](#) **31**, 074102 (2019); <https://doi.org/10.1063/1.5099996>

## SciLight

Highlights of the best new research  
in the physical sciences

AIP  
Publishing

[LEARN MORE!](#)

# Comparison of simulation and experiments for multimode aerodynamic breakup of a liquid metal column in a shock-induced cross-flow

Cite as: Phys. Fluids 31, 082110 (2019); doi: 10.1063/1.5099589

Submitted: 11 April 2019 • Accepted: 26 July 2019 •

Published Online: 16 August 2019



Marco Arienti,<sup>1,a)</sup> Matthew Ballard,<sup>2</sup> Mark Sussman,<sup>3</sup> Yi Chen Mazumdar,<sup>4</sup> Justin L. Wagner,<sup>5</sup> Paul A. Farias,<sup>6</sup> and Daniel R. Guildenbecher<sup>6</sup>

## AFFILIATIONS

<sup>1</sup>Thermal/Fluid Science and Engineering, Sandia National Laboratories, Livermore, California 94550, USA

<sup>2</sup>Department of Mechanical Engineering, Saint Martin's University, Lacey, Washington 98503, USA

<sup>3</sup>Department of Mathematics, Florida State University, Tallahassee, Florida 32306, USA

<sup>4</sup>Woodruff School of Mechanical Engineering, Georgia Institute of Technology, Atlanta, Georgia 30332, USA

<sup>5</sup>Aerosciences Department, Sandia National Laboratories, Albuquerque, New Mexico 87185, USA

<sup>6</sup>Diagnostic Science and Engineering, Sandia National Laboratories, Albuquerque, New Mexico 87185, USA

<sup>a)</sup>Author to whom correspondence should be addressed: [mariant@sandia.gov](mailto:mariant@sandia.gov)

## ABSTRACT

While the mechanisms that drive breakup and aerodynamic dispersion of traditional liquids such as water have been extensively studied, it is not yet clear if models for traditional liquids can be used to accurately describe the behavior of molten metals. In this paper, multiphase simulations with the interface-capturing combined level-set volume-of-fluid approach are used to provide time-resolved morphology and breakup data for a liquid column subject to a shock-induced cross-flow. For the first time, numerical simulation of the behavior of a liquid metal (Galinstan alloy composed of gallium, indium, and tin) is compared to the well-documented behavior of water. Simulations consider a gas cross-flow Weber number between 10 and 12, which produces a multimode breakup morphology consisting of multiple baglike structures. Up to bag breakup, we confirm that the deformation rate of Galinstan follows the same dependence on the gas cross-flow Weber number as ordinary liquids when time is nondimensionalized by including the liquid-gas density ratio. Moreover, we determine that the appearance of a central stem along the column upstream surface in multimode bag breakup is consistent with the occurrence of Rayleigh-Taylor instability. We also resolve bag stretching and fragmentation, to the full extent allowed by our computational resources, and carry out a direct comparison with the measurements of size and velocity of secondary droplets from high-speed digital inline holography. For Galinstan, we illustrate the differences between simulation and experiment that emerge because of the modification of the surface properties of the metal exposed to air.

Published under license by AIP Publishing. <https://doi.org/10.1063/1.5099589>

## I. INTRODUCTION

The study of aerodynamic breakup of liquid sheets, columns, and droplets is crucial for understanding the formation of fuel sprays in engines, liquid dispersion in rain storms, additive manufacturing of metals, thermal spray deposition processes, and many other natural or engineered phenomena. Aerodynamic forces tend to distort the surface of the liquid, while the interfacial surface tension resists deformation. When aerodynamic forces exceed surface tension, the liquid breaks apart into secondary droplets.

Aerodynamic breakup of liquid droplets has been widely investigated for more than a century, with reviews provided by Pilch and Erdman,<sup>1</sup> Guildenbecher *et al.*,<sup>2</sup> Theofanous,<sup>3</sup> and others. For liquids of low to moderate viscosity, many previous investigations indicate that the observable breakup morphologies are most strongly correlated with the nondimensional Weber number,

$$\text{We} = \frac{\rho_G u_{rel}^2 d}{\sigma}, \quad (1)$$

where  $\rho_G$  is the gas-phase density,  $u_{rel}$  is the characteristic gas-to-liquid relative velocity,  $d$  is the characteristic liquid dimension, and  $\sigma$  is the interfacial surface tension. For characterization of temporal behavior, time,  $t$ , is typically nondimensionalized by a characteristic transport time,

$$\tau = \frac{t u_{rel}}{d} \sqrt{\frac{\rho_G}{\rho_L}}, \quad (2)$$

where  $\rho_L$  is the liquid-phase density.

**Figure 1** (Multimedia view) illustrates the flow configuration numerically studied here and first reported in the experiments of Chen *et al.*<sup>4,5</sup> A liquid column is struck by a gas-phase shock wave followed by a nearly one-dimensional convective flow. This leads to an approximate step-change in the relative velocity,  $u_{rel}$ , and creates an aerodynamic pressure distribution that initially deforms the column into an elliptic cross section with the major axis perpendicular to the gas cross-flow direction. Later, nonlinear instabilities result in the formation of complex geometric morphologies and eventual fragmentation into secondary droplets. Note that the column geometry studied here differs from much of the previous fundamental investigations of spherical droplets in cross-flows.<sup>1–3</sup> As discussed in Ref. 5, the column geometry was chosen to reduce diagnostic synchronization challenges. Based on those findings and other previous works,<sup>6–8</sup> the observed breakup structures for impulsively loaded spherical drops and columns follow similar morphological classifications. Therefore, as discussed in detail in the remainder of this work, much of the physical insights drawn here from the column geometry can be extended and compared to previous observations from spherical droplets.

The vast majority of previous fundamental liquid atomization studies have considered ordinary, room-temperature liquids, such as water, alcohols, or hydrocarbon fuels, whose properties span a relatively narrow range ( $\rho_L$  from 700 to 1000 kg/m<sup>3</sup> and  $\sigma$  from 20 to 70 mN/m).<sup>1–3</sup> In contrast, molten metals display roughly an

order-of-magnitude higher density ( $\rho_L \sim 2000$ –7000 kg/m<sup>3</sup>) and surface tension ( $\sigma \sim 400$ –800 mN/m). To compare the breakup behavior of molten metals to that of ordinary liquids, Chen *et al.*<sup>5</sup> performed experiments with Galinstan, which is a nontoxic, eutectic room-temperature liquid metal alloy composed of gallium, indium, and tin. Galinstan has been utilized as a replacement for mercury in thermometers, energy storage research, microfluidics, and flexible electronics.<sup>9</sup> Like many other metals, liquid Galinstan forms an elastic oxide skin<sup>10</sup> with a yield stress that can alter splash impact, breakup, and combustion behaviors.<sup>11</sup> For a discussion of room-temperature gallium-based alloys and their applications, the reader is referred to the review article by Zhao *et al.*<sup>12</sup>

While surface reactivity may be neutralized in inert gases such as argon,<sup>13</sup> this configuration rarely represents natural or manufacturing conditions. Rather, experiments were conducted in air to assess the influence of the oxide skins on breakup. Backlit imaging of water and Galinstan, shown in Fig. 1 (Multimedia view), suggests that the Weber number captures the most critical physics determining the breakup morphologies. There are, however, also differences in the behavior of the two liquids. First, even with the factor  $\rho_L^{1/2}$  in the nondimensionalization of time, as prescribed by Eq. (2), the breakup of the Galinstan column occurs earlier in nondimensional time than water. Next, secondary droplets appear jagged—most likely an indication that metal surface reactivity cannot be ignored at this stage.

Typical experimental results, such as the backlit shadowgraphy images in Fig. 1 (Multimedia view), do not resolve the full three-dimensional (3D) fluid-dynamics and interfacial surface forces that ultimately govern breakup morphologies and production of secondary droplets. This has motivated the creation of highly resolved, 3D computational fluid dynamics (CFD) to simulate multiphase atomization including surface dynamics at resolved gas-liquid interfaces.<sup>14</sup> These methodologies have been applied to gain insight into a number of canonical flows including high-speed liquid injection,<sup>15</sup>

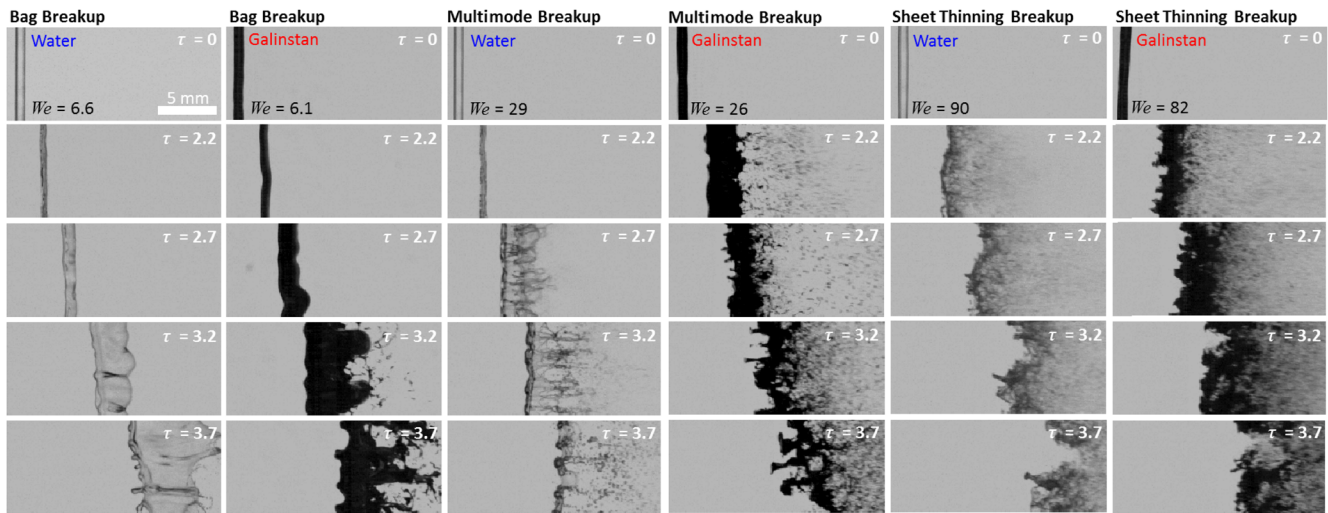


**FIG. 1.** Backlit shadowgraphy of aero-breakup of  $d_0 = 0.84$  mm diameter liquid columns. From left to right, the bag, multimode, and sheet stripping modes are shown at varying Weber numbers. Multimedia view: <https://doi.org/10.1063/1.5099589.1>

**TABLE I.** Properties for water and Galinstan.

Property	Water	Galinstan
Density $\rho_L$ (kg/m <sup>3</sup> )	998	6440
Viscosity $\mu_L$ (mPa s)	0.89	2.4
Surface tension $\sigma$ (N/m)	0.072	0.718

jets in cross-flow,<sup>16,17</sup> liquid sheets,<sup>18,19</sup> jet impingement,<sup>20,21</sup> liquid columns,<sup>22</sup> and spherical drops.<sup>6,23–25</sup>

Historically, validation data set for the aforementioned simulations has been mostly limited to qualitative comparisons to experimental images [similar to Fig. 1 (Multimedia view) data] along with some limited comparisons to secondary drop properties measured downstream of the breakup location.<sup>26,16,21</sup> For the configuration shown in Fig. 1 (Multimedia view), Chen *et al.*<sup>5</sup> presented a number of new experimental methodologies that enhance the resolution of the transient breakup processes. Importantly, time-resolved Digital Inline Holography (DIH) provides detailed measures of column trajectory and shape along with quantification of secondary droplet size and velocity statistics. The current work reports the first numerical simulations of these experiments. Detailed comparison between simulations and experiments improves confidence in the predictions while providing new physical insight.

In addition, the current work performs what is believed to be the first detailed simulation of the aerodynamic breakup of liquid metals. As already mentioned, the experiments of Chen *et al.*<sup>5</sup> reveal differences between the breakup of water and liquid metal Galinstan at nominally the same nondimensional conditions. Simulations are reported to study these differences in more detail. The relevant material properties are reported in Table I. In all cases, the columns are subjected to aerodynamic forces from the surrounding gas with density on the order of 1 kg/m<sup>3</sup>. Consequently, the liquid-to-gas density ratio is on the order of 1000 for water and over 5000 for Galinstan simulations. Such high density ratios are challenging in simulation due to computational costs and numerical instabilities caused by parasitic currents. While some recent simulations have

demonstrated converged solutions at density ratios on the order of 1000,<sup>6</sup> the Galinstan results at density ratios of over 5000 are believed to be the highest density ratios ever reported.

In this work, we examine the morphology of aerodynamic breakup of water and liquid metals at moderate Weber numbers using 3D simulations and compare our findings to experimental results for the same configuration. We assess the ability of models and correlations used for traditional liquids to predict the behavior of liquid metal and assess the impact of neglecting surface reactivity in the current model. Our discussion follows the sequence of events in column breakup: deformation and initial acceleration under cross-flow, emergence of axial and spanwise waves on the liquid column, bag inflation and burst, and finally spray formation. We characterize the resulting droplets, giving their shape and size distributions. Finally, we compare size and velocity distributions for water to experimental measurements to further evaluate our model. Our findings can be used to understand the efficacy of using traditional models and correlations for understanding aerodynamic breakup of liquid metals and to inform decisions on when to include surface reactivity in models.

## II. METHODOLOGY

### A. Experimental methods

Chen *et al.*<sup>5</sup> discussed the experimental configuration, data processing methodologies, and results. The most relevant details are briefly reviewed here, and the interested reader is referred to Ref. 5 for further information. Experiments were conducted in Sandia's Multiphase Shock Tube (MST).<sup>27</sup> This facility uses pressurized nitrogen in a driver section along with a fast-action valve to propagate a planar shock into air at ambient pressure (84.1 kPa in Albuquerque, New Mexico) in the driven section. Figure 2 schematics display the reference coordinate axes that will be used throughout the paper: the positive X axis is in the direction of the shock wave and the gas cross-flow, whereas the liquid column flows along the Y axis into the page. In experiments, the convective flow behind the shock wave was quantified using the pulse-burst particle image

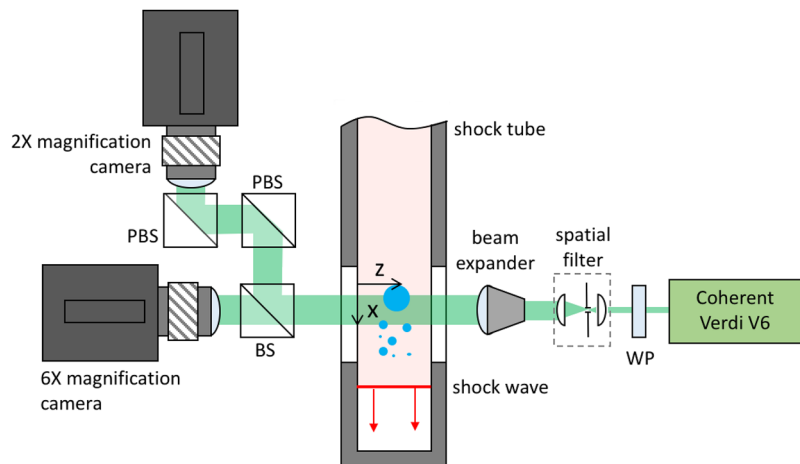


**FIG. 2.** Experimental setup for holographic measurements of liquid breakup inside a shock tube. (WP-wave plate; BS-beam splitter; PBS-polarizing beam splitter).

velocimetry (PIV) configuration detailed in Ref. 27. Breakup morphology was characterized by high-speed imaging, and the droplet size and velocity distribution were quantified by high-speed digital in-line holography (DIH).<sup>4,5</sup> Figure 3 shows an example of a numerically refocused hologram of the water droplets (left), with the resulting droplet tracking for size and velocity evaluation (right). Holograms were collected using two different field of view (FOV) sizes. A 2× magnification FOV was used to obtain time-resolved images at 100 kHz (640 × 280 pixels, minimum detectable diameter 40 μm), while a 6× magnification FOV was used to obtain droplet sizes with a higher dynamic range at 20 kHz (1024 × 1024 pixels, minimum detectable diameter 12 μm).

## B. Numerical approach

One of the objectives of this study is to evaluate the distribution of drops formed immediately after column breakup for direct comparison with the DIH measurements, also taken very close to the point of breakup. The numerical challenge is that the pinch-off process, leading to the formation of a drop, spans several orders of magnitude in space and time, requiring extensive computational resources. In capillary breakup of classical fluids, it has been shown that the dynamics of liquid thread thinning exhibits self-similar behavior under the balance of surface tension, viscous, and inertial forces;<sup>28</sup> this conclusion implies that reference time and length scales shrink to zero in the description provided by the Navier-Stokes equations. In reality, as the liquid thread size reduces to microscopic scale, molecular thermal fluctuations come to control the pinch-off physics.<sup>29</sup> Singular solutions in the run-up to pinch-off are in practice avoided by any stable implementation of a sharp-interface algorithm. As shown early on by Herrmann,<sup>30</sup> in the absence of an explicitly defined breakup length, size distribution diagrams obtained from different grid resolutions are consistent with one another for larger drops but become increasingly divergent as the droplet size becomes comparable to the grid spacing. This dependence cannot be avoided in the interface-capturing simulation framework that is described below and needs to be accounted for in the comparison with experiments.

The multiphase compressible Navier-Stokes equations are solved with the mass-, momentum-, and energy-conserving advection algorithm described by Jemison *et al.*<sup>31</sup> The solution is advanced in time by a semi-implicit pressure update scheme that asymptotically preserves the standard incompressible pressure projection in the limit of infinite sound speed.<sup>32</sup> The computational approach

follows the one adopted for a recent study of primary atomization of n-dodecane<sup>33</sup> and described in Refs. 32 and 31. The region occupied by material  $m = 1, \dots, M$  in a computational cell  $\Omega$  is such that  $\Omega = \cup_{m=1}^M \Omega_m$ . For each material, we solve the following system of equations:

$$(F_m)_t + \nabla \cdot (F_m \mathbf{u}) = F_m \nabla \cdot \mathbf{u}, \quad (3)$$

$$(\rho_m F_m)_t + \nabla \cdot (\rho_m F_m \mathbf{u}) = 0, \quad (4)$$

$$(\rho \mathbf{u})_t + \nabla \cdot (\mathbf{u} \otimes \rho \mathbf{u} + p \mathbf{I} - \boldsymbol{\tau}) = 0, \quad (5)$$

$$(\rho_m E_m F_m)_t + \nabla \cdot (F_m (\rho_m E_m \mathbf{u} + p \mathbf{u} - \mathbf{u} \cdot \boldsymbol{\tau} - k \nabla T)) = 0, \quad (6)$$

where  $F_m$  is the volume fraction,  $E_m$  is the total energy,  $\rho_m$  is the phase density,  $\boldsymbol{\tau}$  is the stress tensor,  $p$ ,  $\mathbf{u}$ , and  $T$  are the flow pressure, velocity, and temperature, respectively. The combined density and conductivity are

$$\rho = \sum_{m=1}^M F_m \rho_m, \quad (7)$$

$$k = \sum_{m=1}^M F_m k_m. \quad (8)$$

The stress tensor,

$$\boldsymbol{\tau} = 2\mu \left( \mathbf{D} - \frac{\text{TR}(\mathbf{D})}{3} \mathbf{I} \right) \quad \mathbf{D} = \frac{\nabla \mathbf{u} + (\nabla \mathbf{u})^T}{2}, \quad (9)$$

depends on the combined viscosity  $\mu$ ,

$$\mu = \sum_{m=1}^M F_m \mu_m. \quad (10)$$

The total energy  $E_m$  and internal energy  $e_m$  are related through the equation

$$E_m = \frac{1}{2} |\mathbf{u}|^2 + e_m. \quad (11)$$

Continuity and momentum equilibrium apply at the gas-liquid interface  $\Gamma$ , of local normal  $\mathbf{n}$  and curvature  $\kappa$ , so that

$$[\mathbf{n} \cdot (\boldsymbol{\tau} - p \mathbf{I}) \mathbf{n}] = \sigma \kappa, \quad \mathbf{x} \in \Gamma, \quad (12)$$

is enforced.

The directionally split Cell Integrated Semi-Lagrangian algorithm (CISL)<sup>31</sup> is coupled with interface reconstruction to preserve the material interfaces while conserving mass, momentum, and energy for each material. In three dimensions, the directional split

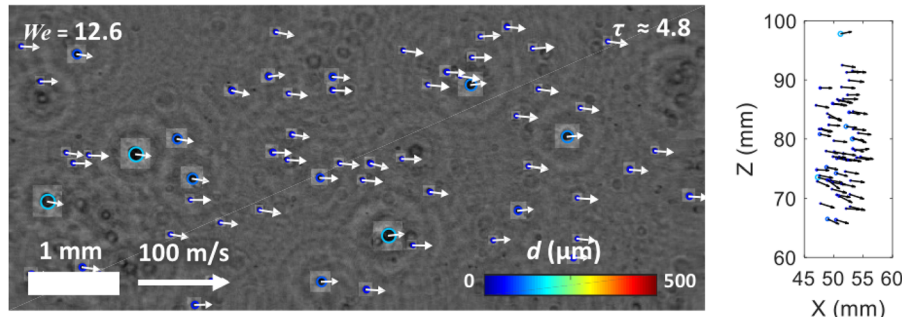


**FIG. 3.** Numerically refocused digital in-line hologram of water droplets after shock-induced breakup. Each droplet is tracked in three dimensions to produce measurements of velocity and droplet size. The lighter boxes around each particle indicate the in-focus Z-location of each droplet. The image on the left shows the view in the X-Y coordinates, and the image on the right shows the tracked droplets in X-Z coordinates.

procedure consists of the following sequence of Eulerian Implicit (EI) and Lagrangian explicit (LE) steps:<sup>35</sup> EI-LE-EI-LE-EI-LE. The CLSVOF slope reconstruction algorithm uses the local level-set and volume-of-fluid values to evaluate the slope and the intercept.<sup>34,36</sup> The level-set function is maintained at each time step as the signed distance to the reconstructed interface. The curvature is evaluated from the level-set function by using the method of heights.<sup>37</sup>

To maintain the separation between different phases in a mixed computational cell, the equation of state is the one belonging to the fluid with the largest volume fraction  $F_m^*$ . This choice is necessary to evaluate the advective pressure,  $P_a(\rho, T)$ , and sound speed,  $c_a(\rho, T)$ , that are required by the compressible flow formulation.<sup>32</sup> The advective pressure of the liquid phase is described for this work by Tait's relation,<sup>38</sup>

$$P_a(\rho) = B \left( \left( \frac{\rho}{\bar{\rho}} \right)^{\gamma} - 1 \right) + A, \quad (13)$$

where the specific properties of the liquid phase are determined by  $\bar{\rho}$ ,  $\gamma$ ,  $A$ , and  $B$ . The corresponding values for the gas phase are derived from the perfect gas equation of state. The square of the sound speed is

$$c_a^2(\rho) = \frac{\gamma B}{\bar{\rho}} \left( \frac{\rho}{\bar{\rho}} \right)^{\gamma-1}. \quad (14)$$

In the following, the values of  $\bar{\rho}$  in Eq. (13) are the reference densities reported in Table I. The other parameters are  $A = 10^5$  Pa,  $B = 3.13 \times 10^8$  Pa, and  $\gamma = 7.15$  for water, and  $A = 10^5$  Pa,  $B = 6.76 \times 10^9$  Pa, and  $\gamma = 7.15$  for Galinstan. The thermal conductivity values used for Galinstan, water, and air are 16.5, 0.614, and 0.0262 W/m K, respectively.

Evaporation is not included in the computational model. At ambient temperature, Galinstan has essentially no vapor pressure.<sup>39</sup> Water evaporation is also relatively slow; we estimate that, even allowing for the maximum possible relative velocity to increase the evaporation rate in dry air, a 10  $\mu\text{m}$  droplet would take 0.017 s to evaporate at 300 K.<sup>40</sup> Larger droplets or more moderate cross-flow velocities correspond to even longer life times, whereas the time scale of the experiments discussed in this work is at most of 0.005 s.

The set of equations described above is discretized on regular Cartesian computational cells, where interface-capturing methods can be implemented most effectively. To reduce the computational requirements while capturing the full scale of the shock-tube experiment, adaptive mesh refinement (AMR) is used to concentrate the computational resources at interfaces such that thin membrane structures and droplet formation are resolved. AMR and data allocation in CLSVOF are managed by the library Boxlib (now AMReX at <https://amrex-codes.github.io/>). AMReX provides a block-structured, hierachic framework to solve general partial differential equations for massively parallel applications.

The AMR procedure is as follows. The coarsest level (level zero) is the Cartesian box covering the whole simulation domain. At every new remeshing operation, a cell-tagging procedure targets the interface; new boxes are combined to cover all of the tagged cells within the assigned coverage efficiency. Data on the fine level are either copied from a previous time step or, when a new box is added, they are conservatively interpolated from the underlying coarse level; the refinement ratio between two consecutive

levels is always two. The new level can in turn be tagged for refinement, and the process is repeated until the input grid resolution is achieved. To avoid interpolation errors from the calculation of the fluxes of mass, momentum, and energy, the tagging function is defined so that the liquid-gas interface is always embedded in the finest grid level. Boxes are distributed amongst processes according to load-balancing strategies such as knapsack and space-filling curve.

Relatively good scaling has been tested with CLSVOF with up to 10 000 MPI processes. The calculations presented in this paper were carried out at Sandia National Laboratories on the supercomputers Red Sky (SUN X6275 2.93 GHz blades with dual socket/quad core configuration and 12 GB RAM) and Sky Bridge (Cray 2.6 GHz Intel Sandy Bridge with 64 Gb RAM/node), both with InfiniBand interconnect.

### C. Convergence study

Since membrane stretching and bursting is the dominant characteristic of the aerodynamic breakup investigated in this paper, it is important to understand the capabilities and limitations of interface-capturing in this context. The convergence study presented in this section was carried out in two dimensions, as the properties of interface reconstruction can be illustrated equally well and at smaller cost compared to 3D simulations. The case discussed here, at Mach number  $M = 1.15$ , corresponds to the breakup mode that will be considered in comparison with experiments later on.

Figure 4 displays the liquid surface immediately after the first breakup for increasing grid refinement, which is detailed in Table II. The snapshots are chosen to correspond as much as possible to the same instant of membrane breakup. The coarsest grid resolution is  $d_0/\Delta x = 16$ , where  $d_0$  is the initial diameter of the fluid column and  $\Delta x$  is the grid spacing. Increasing grid refinement supports the numerical membrane representation as it stretches and reaches the critical thickness of one or two computational cells. As a result, the time at which the membrane begins to burst, labeled  $t_b$ , increases with increased grid refinement, allowing the membrane to become more inflated. Due to the increase in drag of the cross section, the cross section location shifts further downstream.

As seen in Table II, the difference in  $t_b$  between each two consecutive cases decreases almost monotonically, from 0.08 ms to 0.03 ms, showing that  $t_b$  converges under grid refinement. Furthermore, Fig. 4 shows that the main features of the membrane remain the same at every grid resolution considered. A central stem separates two thinner portions of the column that inflate and become concave with respect to the incoming flow. The edges terminate into a thickened cross section resembling a rim. The edges of the cross section correspond in three dimensions to the toroidal rim that forms in the aerodynamics breakup of a droplet after it has taken its saucer-shaped disc.<sup>1-3</sup> Lacking inflow perturbations, the first point where the membrane bursts is located in the same position, approximately at the midpoint between the stem and the rims. Small satellite droplets form there and are advected downstream. Once the first breakup occurs, the gas cross-flow is given a way through, membrane inflation stops, and recoil due to surface tension begins.

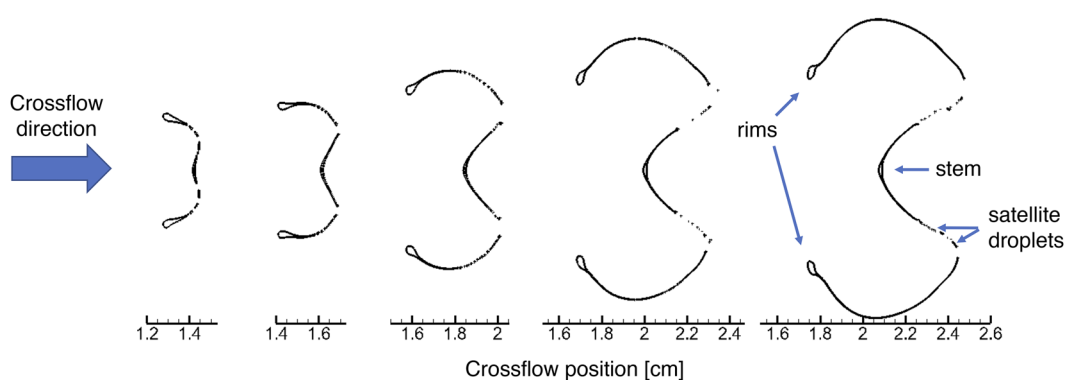


**FIG. 4.** Liquid surface in 2D multimode breakup immediately after membrane bursting as a function of grid resolution ( $d_0/\Delta x = 16, 32, 64, 128$ , and  $256$  from left to right). The x-axis marks the current position from the initial location at  $X = 0.6$  cm.

#### D. Computational setup for 3D simulations

The computational domain for the Galinstan and water 3D simulations is a  $32 \times 24 \times 8$  mm $^3$  box corresponding to a base block of  $384 \times 288 \times 96$  Cartesian cells. The initial diameter of the column is  $d_0 = 0.94$  mm, and the total simulation time is 5 ms. Three more levels of refinement are added to the base grid to capture features of interest as they develop over the course of the simulation, reaching an effective grid resolution of  $2.6\text{ }\mu\text{m}$ . Based on the previous convergence study, the corresponding ratio  $d_0/\Delta x = 45$  is considered an acceptable compromise with respect to the available resources, providing sufficient resolution of the breakup morphology even if biased toward a more limited membrane development. No turbulence model was deemed necessary because of the low Reynolds number and the low inlet turbulence of the experiments. The water column case reached the peak value of  $92.6 \times 10^6$  cells, and the Galinstan case reached  $80 \times 10^6$  cells.

The reference frame of the simulation is the lab frame, so the column can freely move downstream under the effect of the gas cross-flow. Boundary conditions are set to correspond to the shock tube conditions. At a low Mach number, the measured cross-flow velocity in the MST, shown by the continuous line in Fig. 5, increases smoothly, rather than with an ideal-step change, to the postshock value. The same velocity  $U_2(t)$  is used to set a time-dependent inlet boundary condition for water ( $U_2$  is assumed to be constant after 3.5 ms). Inlet pressure and temperature are derived from  $U_2(t)$  using 1D shock theory<sup>38</sup> with the preshock pressure and density conditions of 841 kPa and  $0.976$  kg/m $^3$ .

The gas cross-flow velocity of  $\bar{U}_2 = 30$  m/s is taken as a reference for the simulation with the water column. Based on the properties of Table I, the estimated Weber number is  $\text{We} = \rho_{g,2}\bar{U}_2^2 d_0 / \sigma = 12.6$ ,

**TABLE II.** 2D convergence study at conditions similar to the full 3D cases discussed later:  $t_b$  is the earliest detected time of membrane bursting. In the first row, the diameter of the undeformed cross section is divided by  $\Delta x$ , the effective spacing on the Cartesian grid.

$d_0/\Delta x$	16	32	64	128	256
$t_b$ (ms)	1.03	1.11	1.21	1.27	1.30

where  $\rho_{g,2}$  is the gas density after the passage of the shock. The corresponding Reynolds and Mach numbers are listed in Table III. The last column of the table reports small values of Ohnesorge number for both liquids.

The inlet conditions for Galinstan were found from a set of simulations carried out on the base grid (without adaptive mesh refinement) by increasing the cross-flow velocity; we found that  $\bar{U}_2 = 80$  m/s yielded deformation and breakup modes that were comparable with the ones observed for water. To maintain consistency with the water simulation, the velocity profile was scaled up as shown in Fig. 5, dashed line (even though the actual velocity profile is steeper given the higher Mach number, see the work of Chen *et al.*<sup>5</sup>). Since the rest of the conditions are the same as in the case with water, the postshock density for the simulation with Galinstan is slightly larger; the surface tension of Galinstan is also larger so that the resulting Weber number is actually lower than for water:  $\text{We} = 10.2$ .

Symmetric boundary conditions were applied in the transverse direction with respect to the liquid column ( $Z$  direction). Periodic boundary conditions were applied in the  $Y$  direction, with the understanding that waveforms that develop along the liquid column will be affected by the periodicity constraint. At  $t = 0$ , the column was modeled as a cylinder with  $Y$ -velocity of  $v_j = 12$  m/s for water and  $v_j = 4$  m/s for Galinstan. These two values remained essentially constant for the duration of the simulations. Finally, the zero

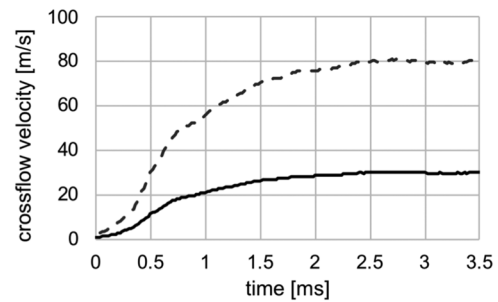


**FIG. 5.** Reference inlet velocity profile. Continuous line: measured in the shock tube facility for the simulation of the water column; dashed line: inlet velocity used for the simulation of the Galinstan column.

**TABLE III.** Simulation conditions. The initial column diameter was  $d_0 = 0.94$  mm in both cases.

Liquid	Peak gas velocity $U_2$ (m/s)	Peak gas density, $\rho_{g,2}$ (kg/m <sup>3</sup> )	Weber number (We)	Reynolds number (Re)	Mach number (M)	Ohnesorge number (Oh)
Water	30	1.06	12.6	1600	1.0534	0.0034
Galinstan	80	1.22	10.2	4900	1.1478	0.0012

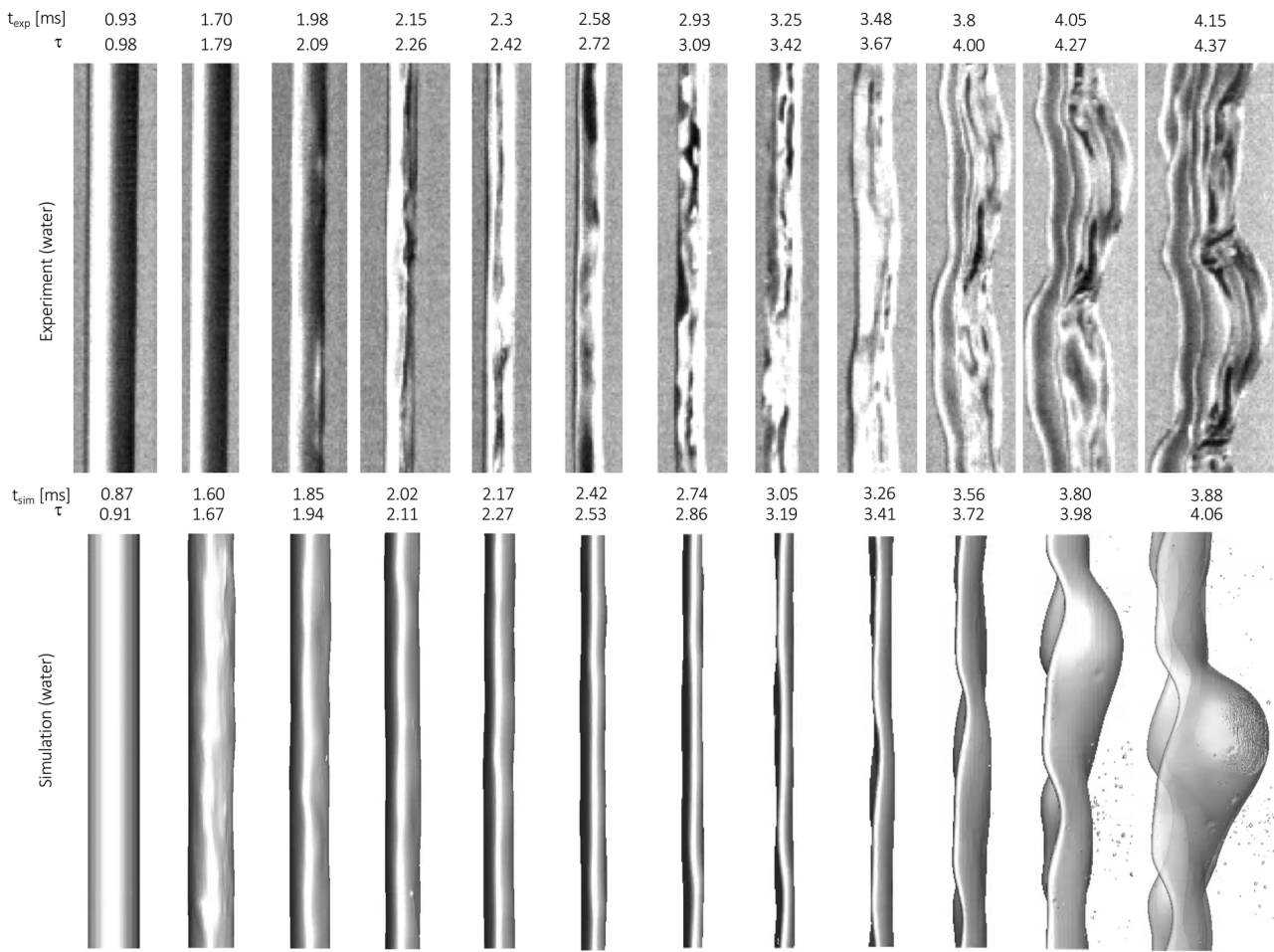
gradient condition for pressure was maintained at the outlet to mimic outflow conditions.

### III. RESULTS AND DISCUSSION

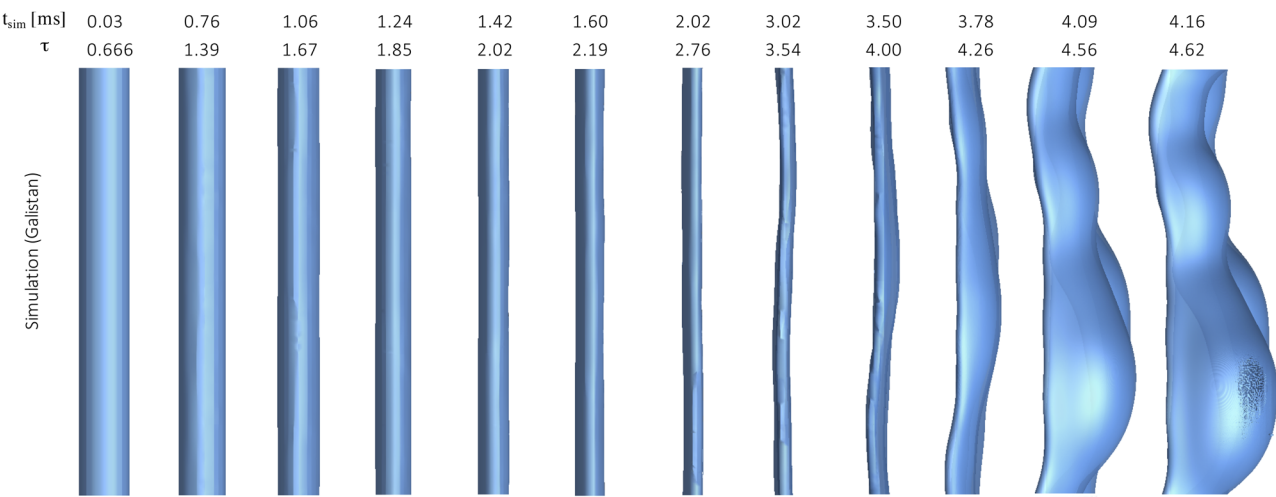
#### A. Visual comparison

Figure 4 compares selected frames from the backlit images of water breakup with volume renderings from the simulation at approximately corresponding times. The view is in the Z direction

and perpendicular to the cross-flow, which occurs from left to right. All images are cropped to the same field of view to show that the simulation captures both the axial and spanwise deformation of the column. To synchronize the time references of experiments and simulations, a delay of 55 frames at 100 000 fps (0.55 ms) is added to the laboratory images; the delay was estimated based on the trigger level of the experiment. Simulation renderings for Galinstan are displayed in Fig. 7 (Multimedia view) with snapshots taken at approximately the same values of nondimensional time as in Fig. 6



**FIG. 6.** Backlit images from the MST compared to volume renderings of zero level-set isosurfaces for water. The gas flows from left to right, and the liquid flows from top to bottom. The initial column diameter is  $d_0 = 0.84$  mm in the experiment and  $d_0 = 0.94$  mm in the simulation. All images are cropped to the same field of view. Multimedia views: <https://doi.org/10.1063/1.5099589.2>; <https://doi.org/10.1063/1.5099589.3>



**FIG. 7.** Volume renderings of zero level-set isosurfaces for the Galinstan column. The gas flows from left to right, and the liquid flows from top to bottom. The initial column diameter is  $d_0 = 0.94$  mm in the simulation. All images are cropped to the same field of view as in Fig. 6. Multimedia view: <https://doi.org/10.1063/1.5099589.4>

(Multimedia views). The two sequences show the same series of events: the undisturbed cylindrical column flattens in the cross-flow direction, taking an approximately elliptical shape; small perturbations begin to appear on the column surface; the perturbations become more coherent and regularly spaced so that the column sides are increasingly sinuous; eventually, multiple bags appear at the trailing edge of the column and begin to inflate. The various aspects of column deformation that precede bag breakup are quantified and discussed in Secs. III B–III E.

## B. Early-stage trajectory

In the early phases of column deformation, the translation and deformation of the intact liquid column can be observed and tracked using simple image processing routines. Holography data for water and Galinstan columns have already been reported in Ref. 5, where the  $X$ -position of the leading edge (e.g., the windward side of the column) and the apparent column width are tracked with respect

to the nondimensional time  $\tau$ . The values plotted in Fig. 8 are the spanwise averages of the leading edge profiles as they are evaluated within the field-of-view of the experiment and of the simulation; the error bars correspond to the standard deviation of the leading edge profile with respect to its position averaged in the  $Y$  direction. The amplitudes of the error bars are initially small, but at later times the leading edge begins to assume a pronounced wavelike shape, as shown in Figs. 6 and 7 (Multimedia views), which increases the standard deviation.

We plot the results from three different tests with water and Galinstan at the same nominal conditions to illustrate the run-to-run variability in the experiment. Slightly different flow conditions can be obtained at the inlet of the test section depending on how quickly the shock tube valve opens. This effect is more pronounced at low Mach numbers, such as the case considered here, because the MST was designed for higher Mach number conditions. In the comparison with the simulation, Fig. 8(a) shows that after  $\tau = 2.2$  the leading edge of the water column accelerates faster than in the

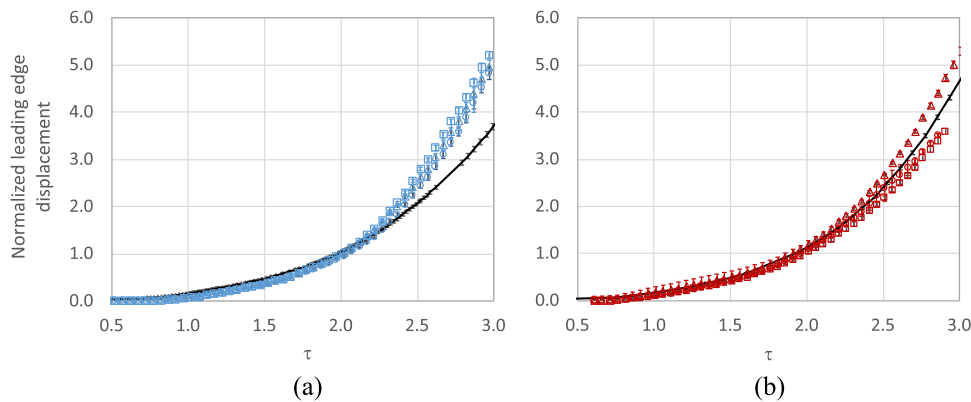


**FIG. 8.** Comparison between the leading edge trajectory from simulation (black symbols and line) and experiment for (a) water (experiment—blue symbols) and (b) Galinstan (experiment—red symbols). The leading edge position is normalized by  $d_0$ .

simulation. We still do not have a satisfactory answer to explain this difference, but we note that in a similar plot reported in Ref. 5, the water column at  $We = 13$  had already been identified as an outlier with respect to the cases at higher Weber numbers. Conversely, the leading edge trajectory for Galinstan collapses with the other curves in Ref. 5 and agrees well with the simulation in Fig. 8(b).

Coupled with the displacement of the column in the cross-flow direction is its deformation under the action of aerodynamic forces, which in turn determines how fast the column accelerates downstream. In Fig. 9, the column deformation is given by plotting the distance between the leading and trailing edges of the column. As in Fig. 8, three different test runs are plotted, and the error bars correspond to the deviation with respect to the average width value within the field-of-view for each run and simulation.

Column flattening corresponds to the deformation of the circular cross section to an oblong shape. What follows is not necessarily a return to the circular cross section, except at very low Weber numbers. Rather, bulges and bags begin to appear on the stretched surface of the column that substantially increase the apparent width. It is the trailing edge that mostly reflects the deformation of the column, a point clearly illustrated by the sequence of images in Figs. 6 and 7 (Multimedia views).

The difference between the individual tests is more tangible in the column width diagram than in the leading edge trajectory. For water, the measured minimum width of the column is  $0.6 d_0$  in one test, but it is closer to  $0.4 d_0$  in the other two. For Galinstan, the minimum width is between  $0.5 d_0$  and  $0.6 d_0$  for all three tests. The time of minimum column width, which can be identified as a marker for the beginning of bag formation, similarly differs between tests. For water, this occurs at approximately the same time in the simulation and in two of the three experiments, at  $\tau \sim 2.4$ , but much earlier in the third, at  $\tau \sim 1.7$ . There seems to be more uniformity for Galinstan, with the minimum width achieved between  $\tau \sim 2.2$  and  $2.4$ . Even accounting for these differences, the simulations differ from the experiments in the rate of bag development, which is substantially larger in the experiments. In the Galinstan simulation, bag formation is delayed to the point that the column width continues to decrease to almost  $0.3d_0$  past  $\tau \sim 3$ . The discrepancy points to an apparent difficulty for the model to initiate membrane stretching, possibly because of the lack of small turbulent fluctuations in the gas phase that could perturb the column surface. In the case of Galinstan, changes in the coefficient of surface tension due

to surface reactivity are not modeled (for gallium-based alloys, the oxygen tends to increase surface tension; see Ref. 12 and the references therein). Additional diagnostics are needed to identify the root cause of this problem, and at this moment, we can only point to the good agreement of the simulation results up to the moment of bag formation.

### C. Column deformation and drag coefficient

It is of particular interest to combine data from the column deformation and its center of mass trajectory to evaluate the drag coefficient as a function of time. The drag coefficient  $c_d$  in the cross-flow direction is derived from the definition

$$ma_x = \frac{1}{2} c_d A_f \rho_g (U_2 - v_x)^2, \quad (15)$$

where  $A_f$  is the frontal area,  $U_2$  is the cross-flow velocity from Fig. 5, and  $v_x$  is the column bulk velocity (the velocity of its center of mass).

The remaining parameters are derived from the following analysis. Based on simulation data, the distance of  $7d_0$  from the rest position is crossed in approximately 3.4 ms, corresponding to a constant acceleration  $a_0 = 2x/t^2 = 1140 \text{ m/s}^2$ . A more accurate evaluation of acceleration is obtained by twice differentiating the center of mass position as a function of time. The frontal area is directly evaluated from snapshots of the simulation taken from the cross-flow direction, that is, by applying edge identification to a sequence of images analogous to the ones in Figs. 6 and 7 (Multimedia views). Local fluctuations of the frontal area for  $\tau > 2.5$  make it difficult to treat the column with this approach, and eventually, the column loses cohesion via bag breakup. After applying a smoothing procedure (“rlowess” in Matlab<sup>41</sup>) to reduce noise, we find that the acceleration is a growing (but nonmonotonic) function of time in the interval of interest.

The resulting values of  $c_d$  as a function of  $\tau$  are plotted in Fig. 10 for water and Galinstan. While surface mobility and internal circulation could be affecting drag, we find that, at these cross-flow conditions, the drag coefficients for both liquids are approximately close to unity after the passage of the shock. This value is consistent with  $c_d$  of a rigid cylinder at Re numbers between  $10^2$  and  $10^5$ .<sup>42</sup> We find that  $c_d$  increases to two when the column cross section deforms from circular to elliptical, although this is an approximate estimate

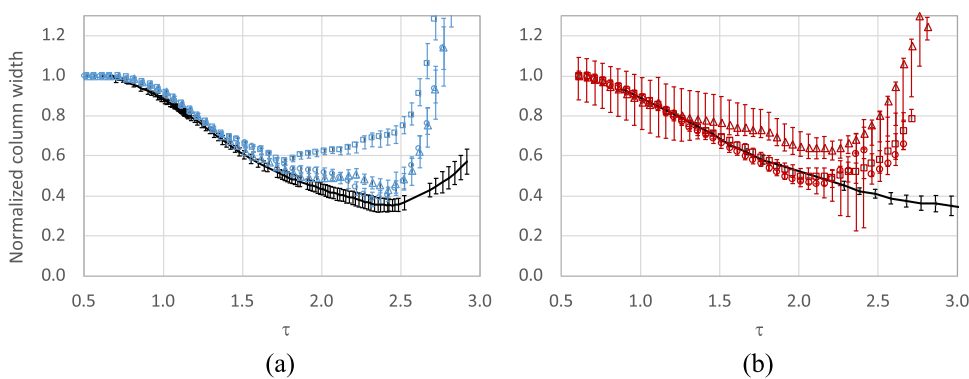


**FIG. 9.** Nondimensional column width from simulation (black symbols) and experiments for (a) water (experiments—blue symbols) and (b) Galinstan (experiments—red symbols). The width is normalized by  $d_0$ .

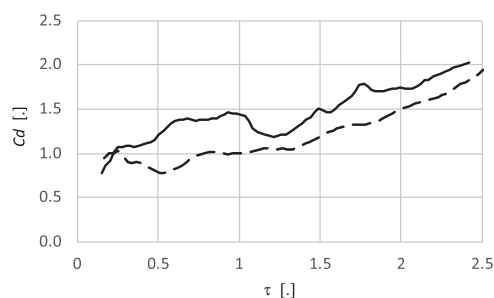


**FIG. 10.** A posteriori evaluation of the cross-flow drag coefficient for water (continuous line) and Galinstan (dashed line).

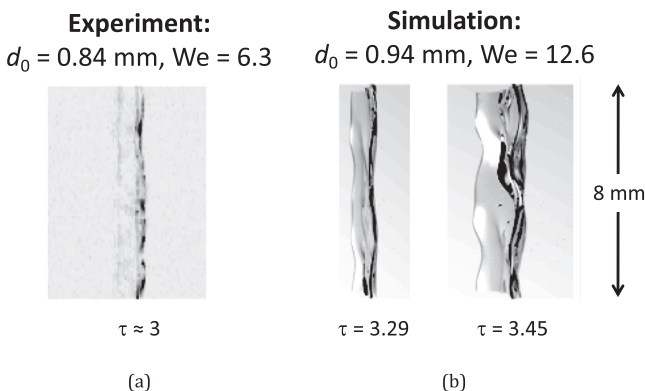


**FIG. 11.** Wave propagation along the water column. The surface features visualized in the experiment (a) correspond in the simulation to the formation of bag edges (b).

that may overshoot the actual values due to the amplified noise in the calculation of the column acceleration. As a reference, the value of 1.8 is found in the literature for a plate normal to the flow at  $\text{Re} = 10^4$ .<sup>42</sup>

#### D. Axial waves

Perturbations are observed to form and grow along the liquid column during the process leading to bag breakup. **Figure 11(a)** shows a backlit picture of the water column taken during the early time of bag formation. In **Fig. 11(b)**, the ray-tracing rendering of the computed liquid surface at similar illumination conditions suggests that the darker features seen there are due to the thickening and rounding of the column edges. The simulation shows with clarity that the leading edge displayed in the backlit images of **Fig. 1** (Multimedia view) is actually the visual superposition of the two edges at the sides of the column.

Edge thickening is accompanied by the formation of wavelike features in the axial ( $Y$ ) direction of the column. These features are more clearly visible in the frontal column view of **Fig. 12** (Multimedia view) for water and **Fig. 13** (Multimedia view) for Galinstan, where the column surface is colored by the axial component of its surface unit normal vector to enhance the sense of depth. The time intervals of the two sequences are chosen so that the spanwise width of the column ( $Z$  direction) is similar in the two cases. The blue lines are added to track salient wave features between one frame and the next, as they are advected downward along the column. For the water column, the dominant wavelength along the edges is smaller than 4 mm, whereas for Galinstan the wavelength is almost exactly 4 mm (the length of the column displayed in the field-of-view is approximately 8 mm). Unfortunately, a more quantitative wavelength analysis is limited by the small extension of the computational domain in the  $Y$  direction.

As time proceeds, the time sequence in the two plots shows that the depressions of the liquid surface—concave with respect to the incoming cross-flow—become deeper and more rounded, while the bulges emerge as ligaments separating the bags. A central stem begins to form parallel to the two edges, and it is particularly visible in **Fig. 13** (Multimedia view). In simulations at lower Weber numbers not shown here, the central stem does not form, whereas at higher Weber numbers, the edges accelerate more than the bulk of the column and bag formation is suppressed (the reader is referred to Ref. 43 for a gallery of cross-sectional shapes at different Weber numbers).

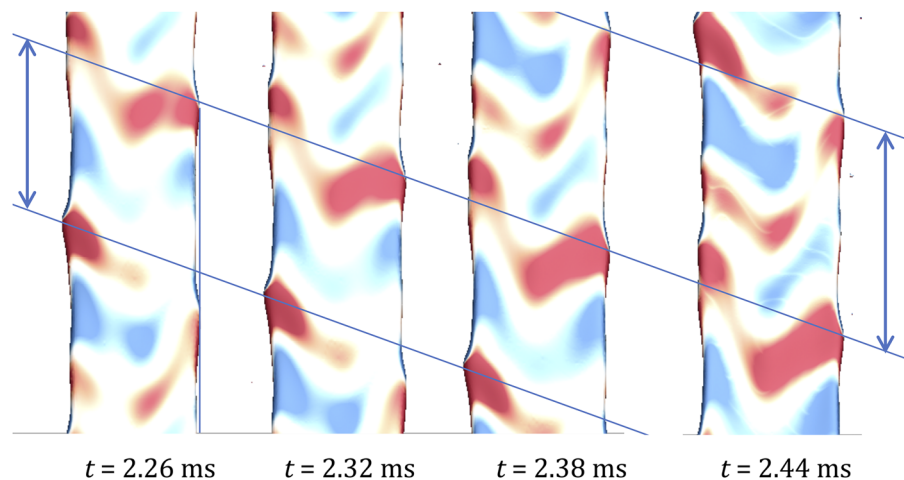


**FIG. 12.** Front view of the water column seen from the direction of incoming cross-flow, colored by the  $Y$ -component of the surface normal from -0.2 (blue) to +0.2 (red). Also shown is the approximate spacing of the edge deformation. Multimedia view: <https://doi.org/10.1063/1.5099589.5>

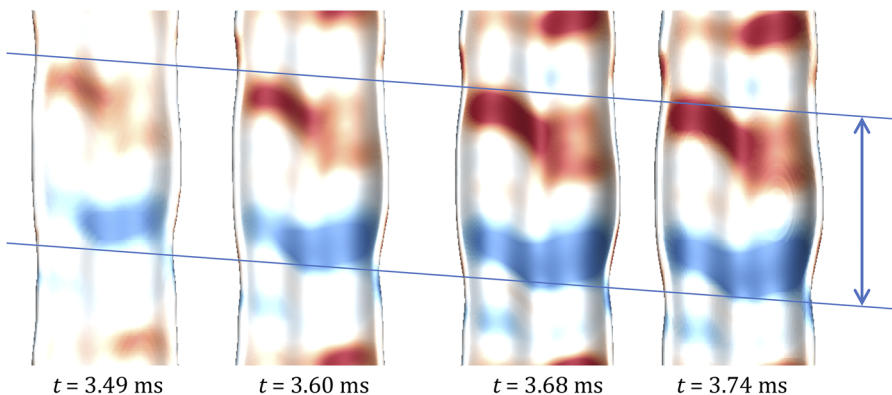


**FIG. 13.** Front view of the Galinstan column seen from the direction of incoming cross-flow, colored by the Y-component of the surface normal from  $-0.2$  (blue) to  $+0.2$  (red). Also shown is the approximate spacing of the edge deformation. Multimedia view: <https://doi.org/10.1063/1.5099589.6>

To interpret the above observations, we recall that in spherical drops the bag-stamen and dual-bag breakup modes can be interpreted as a result of Rayleigh-Taylor instability (RTI), as suggested by Zhao *et al.*<sup>44,45</sup> for low-viscosity liquids. The critical condition is for drop diameter to be larger than the critical wavelength,

$$\lambda_{cr} = 2\pi \sqrt{\frac{\sigma}{\rho_L a}}, \quad (16)$$

where  $a$  is the acceleration of the droplet and the additional term due to the gas density is dropped because of the large  $\rho_L/\rho_G$  ratio. The wave number of the most unstable mode, according to the linearized stability analysis for 2D flow, is  $\sqrt{3}\lambda_{cr}$ .<sup>46</sup>

We apply this analysis to both the axial ( $Y$ ) and spanwise ( $Z$ ) directions of the column. An exact estimate of  $\lambda_{cr}$  is made difficult by the fact that the column acceleration is not uniform; however, we can assume that the acceleration is approximately the same for the water and the Galinstan cases. Thus, from Table I and taking  $a_0 = 1140 \text{ m/s}^2$  from our previous estimate, the calculated critical wavelength for water,  $\lambda_{cr} = 1.58 \text{ mm}$ , is shorter than  $\lambda_{cr} = 1.96 \text{ mm}$  for Galinstan. This result agrees with our observation of shorter surface wavelengths for water with respect to Galinstan. It also suggests that a different ratio of fluid properties,  $\sqrt{(\sigma/\rho_L)}$  from Eq. (16), intervenes in deciding whether the mode of breakup includes a single spanwise bag or multiple bags; we recall that in the early stages of column deformation, the scaling parameter was instead  $\sqrt{(\rho_G/\rho_L)}$ .

Linear instability analysis applies only to the initial stage of the column deformation, when the perturbation amplitudes are small. By  $\tau = 3.3$ , secondary ligaments perpendicular to the central stem become visible, and the most prominent bag can be easily identified in the last frame of Fig. 6 or 7 (Multimedia views) as it is beginning to burst.

### E. First membrane breakup

The progression to bag breakup is illustrated by the snapshots of Fig. 14 for the two liquids. For water, the membrane tears at multiple locations, forming a spray of tiny droplets and a loose weblike structure of ligaments and holes; each small membrane hole opens quickly and allows droplets to bead up along the edges. The resulting droplet size distribution is not monodisperse, as can be inferred from the range of downstream droplet positions in the cross-flow direction in Fig. 14(a).

In the Galinstan simulation, the membrane burst occurs in a more orderly fashion. Starting from the point of minimum thickness, the central part of the membrane disintegrates rather uniformly, forming a more monodisperse distribution, as seen in

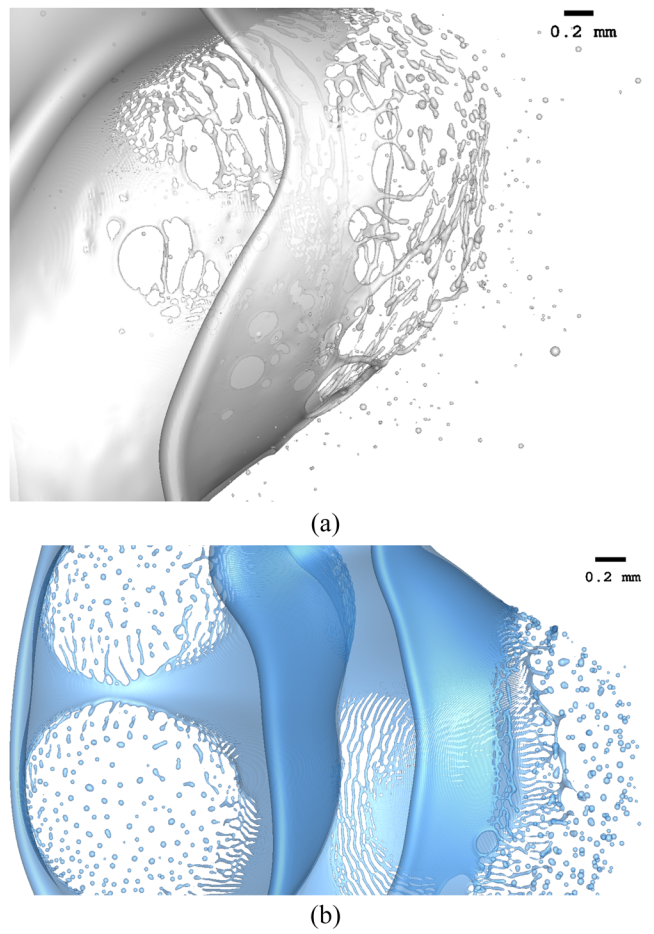


**FIG. 14.** Partial side view of the column from the simulations with a close-up of membrane breakup: water at  $t = 3.444 \text{ ms}$  (a) and Galinstan at  $t = 4.293 \text{ ms}$  (b). Gas cross-flow is from left to right, and column flow is from top to bottom.

Fig. 14(b). Compared to water, the unbroken part of the Galinstan membrane has a tighter arrangement of ligaments: formed by draining of the surrounding liquid elements, these ligaments advance into the membrane while their tips are undergoing capillary breakup.

Figure 15 shows the same column close-up of Fig. 14 but seen from the axial (Y) direction. Also plotted in the diagram are the velocity vectors of the individual droplets as they are forming from membrane breakup; included are a few early detached droplets that have escaped the wake of the column and are accelerating to the cross-flow gas velocity. It would seem that in the simulation the Galinstan column possesses a more uniform membrane thickness than water. This could be due to its larger inertia compared to water, which makes a Galinstan membrane less susceptible to fluctuations in gas dynamic pressure.

The images of the Galinstan column reported in Ref. 5 exhibit the same combination of dispersed droplets and fragmented membranes that can be observed in Figs. 14(b) and 15(b): stringlike structures, forming at the periphery of the burst membranes, can similarly be identified from the backlit photographs as they are in the simulations. However, this is where the similarities stop. As shown in the work of Chen *et al.*,<sup>5</sup> the bag breakup of Galinstan does not manifest as beading. Instead, the membranes break open along fracture lines, akin to fractures seen in solid mechanics, and their ligaments exhibit sharp edges, consistent with the rapid oxidation at the surface of the metal. These effects could not be predicted by the Galinstan simulation since no dependence of the surface tension coefficient on the liquid surface state, nor any fracture model, was implemented into the code.

In recalling that the Galinstan column deformation behaves similarly in experiments and simulations up to the point where the membrane breaks and ejects droplets, it is reasonable to conclude that only at this time do substantial differences between a traditional

liquid such as water and molten metal begin to appear. Eventually, the fractured sections of the membrane are ejected as nonspherical droplets, but surface oxidation prevents smaller droplets from reaching spherical, minimum energy shapes over time. In Sec. III F, the analysis of drop size and shape distribution is considered in light of the above observations.

#### F. Procedure to extract droplet size and shape distribution

Immediately after a membrane bursts, a group of small liquid structures is observed that are either spherical droplets or ligaments in the process of subdividing in droplets. High-speed DIH provides time-resolved measurements of these droplet fields that can be directly compared with simulation results. To postprocess simulation data for droplet characteristics, the zero isosurface of the liquid-gas level set (the liquid surface) is transformed into a tessellation made of triangular and quadrilateral faces. A recursive procedure then separates the liquid into structures, or “blobs,” made up of faces that share common nodes. Each blob corresponds to a droplet, a liquid ligament, or an intact portion of membrane. The number of connected faces defining the surface of each blob may vary from several thousand to a few tens. The exclusion of polyhedra with less than 16 faces ensures that extreme cases of under-resolved liquid structures are discarded.

Two quantities that are immediately available from this procedure are the volume and the surface area of each polyhedron,  $V$  and  $S$ , respectively; from those values, the diameters of the volume-equivalent and surface-equivalent sphere are

$$D_V = \left( \frac{6V}{\pi} \right)^{1/3}, \quad D_S = \left( \frac{S}{\pi} \right)^{1/2}. \quad (17)$$

For a collection of  $N$  blobs with  $\{D_{V,i}\}$ ,  $\{D_{S,i}\}$ ,  $i = 1, \dots, N$ , the Sauter mean diameter is

$$\text{SMD} = \frac{\sum_i D_{V,i}^3}{\sum_i D_{S,i}^2} = 6 \frac{\sum_i V_i}{\sum_i S_i}. \quad (18)$$

In addition to the SMD, the ratio  $D_V/D_S$  provides an indication of how far a blob is from the spherical shape. This is because for a geometrical shape  $D_V \leq D_S$ , whereas  $D_V = D_S$  only for a sphere. The  $D_V/D_S$  ratio can therefore be used to characterize the deformation of a ligament from the spherical shape.

The characterization of droplet statistics via DIH is different in that it calculates droplet diameter from the projected area. This method provides a third indicator of size,

$$D_{2D} = \left( \frac{S_{proj}}{\pi} \right)^{1/2}, \quad (19)$$

where  $S_{proj}$  is the projected area of the droplet along the direction  $\mathbf{n}_{proj}$ . For a droplet discretized as an  $m$ -faced polyhedron, the projected area can be evaluated from

$$S_{proj} = \sum_{j=1}^m \max(\mathbf{A}_j \cdot \mathbf{n}_{proj}, 0), \quad (20)$$

where  $\mathbf{A}_j$  is the face normal directed toward the interior of the polyhedron with magnitude equal to the area of the surface. The SMD of

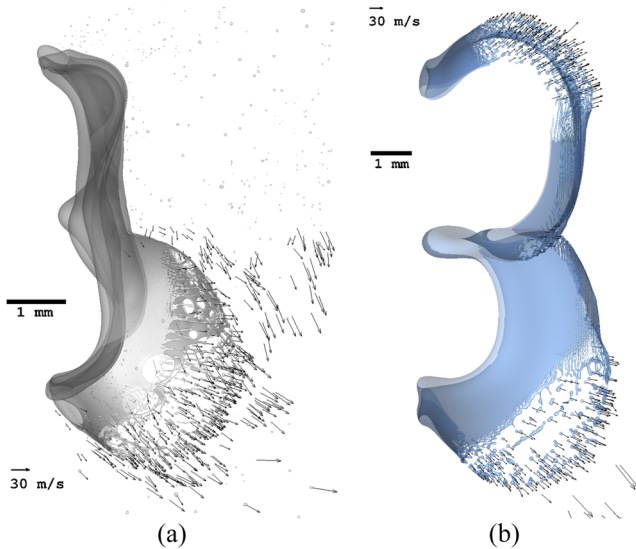


**FIG. 15.** Top view of the column from the simulations: water at  $t = 3.444$  ms (a) and Galinstan at  $t = 4.293$  ms (b). The velocity vectors of the individual droplets formed from membrane breakup are shown. Gas cross-flow is from left to right and column flow is into the page.

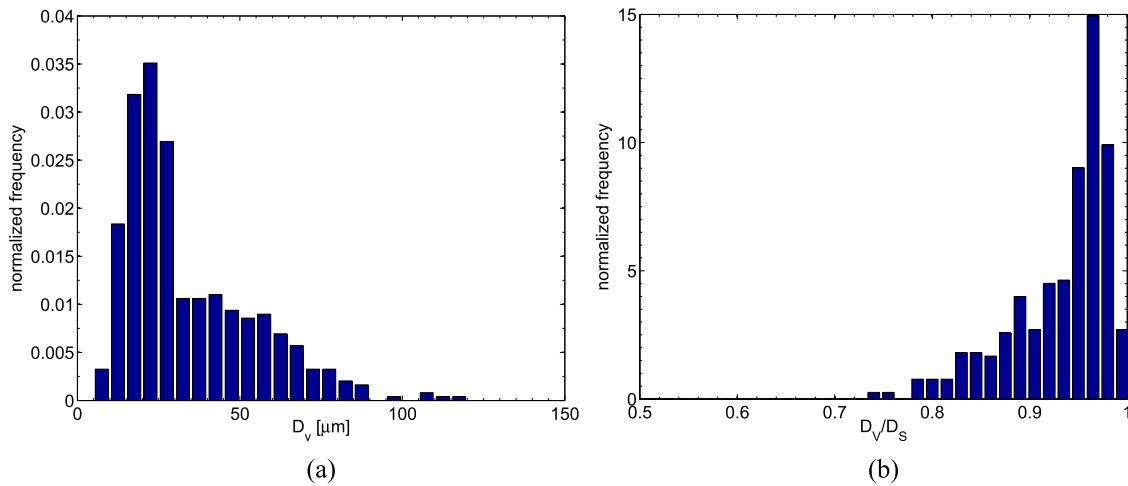


**FIG. 16.** Droplet statistics from simulation for water after first membrane burst: (a) size distribution of volume-equivalent spheres (5  $\mu\text{m}$  bin width) and (b) ratio distribution of volume-equivalent and surface-equivalent diameters (0.015 bin width). 490 samples were used.

surface-equivalent projected drops is then

$$\text{SMD}_{2D} = \frac{\sum_i D_{2D,i}^3}{\sum_i D_{2D,i}^2}. \quad (21)$$

Simple geometric considerations suggest that  $\text{SMD}_{2D} > \text{SMD}$  when not all of the droplets are spherical. This situation occurs, for instance, in the membrane burst depicted in Fig. 14, where several elongated ligaments can be observed. From those snapshots, the normalized frequency distributions of  $D_V$  and of the deformation ratio  $D_V/D_S$  are displayed in Fig. 16 for water and in Fig. 17 for Galinstan. Because the SMD value is dependent on the chosen method of calculation if the sample population is not composed of spherical particles, we expect that the SMD derived from the

particles' projected area will be a higher bound of the actual SMD.

To illustrate this postprocessing procedure, Fig. 16 shows the normalized size and deformation distribution for water, after the first membrane burst. Frame (a) indicates that the majority of droplets are of size  $10 < D_V < 80 \mu\text{m}$ , with a peak value around  $22.5 \mu\text{m}$  and  $\text{SMD} = 49.4 \mu\text{m}$  from Eq. (18). Since the smallest grid resolution is  $\Delta x = 2.6 \mu\text{m}$ , we can expect that some of the droplets that are smaller than  $\sim 5-10 \mu\text{m}$  will not be captured by the simulation. Frame (b) shows that most of the droplets are elongated at this time because the peak frequency of the deformation ratio is reached at  $D_V/D_S = 0.965$ . The SMD based on the projected area, Eq. (21), can therefore be expected to be larger:  $\text{SMD}_{\text{top}} = 63.5 \mu\text{m}$  from the top view and  $\text{SMD}_{\text{side}} = 78 \mu\text{m}$  from the side view.

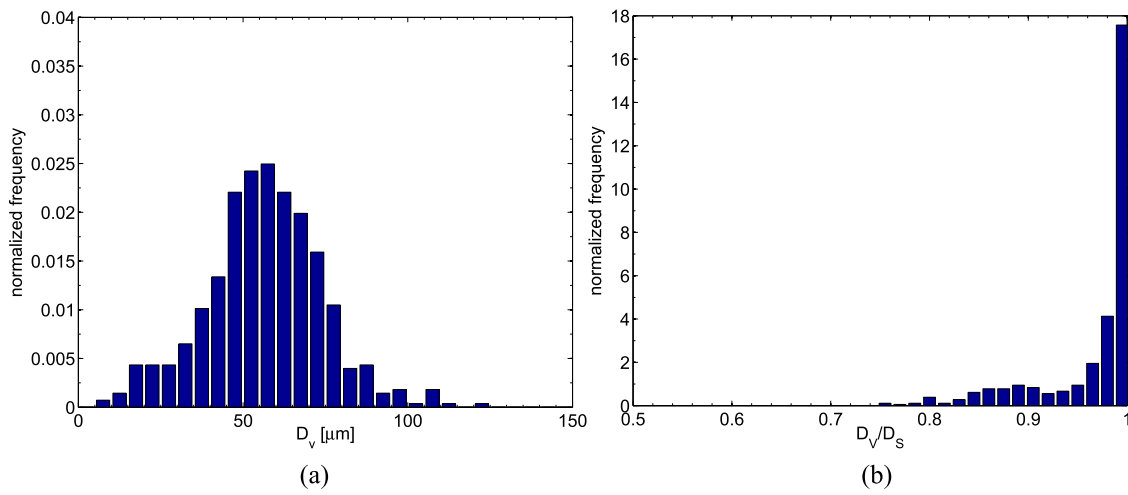


**FIG. 17.** Droplet statistics from simulation for Galinstan after first membrane burst: (a) size distribution of volume-equivalent spheres (5  $\mu\text{m}$  bin width) and (b) ratio distribution of volume-equivalent and surface-equivalent diameters (0.015 bin width). 553 samples were used.

In Fig. 17, frame (a), fewer small droplets are observed for Galinstan and most fall in the  $30 < D_v < 75 \mu\text{m}$  range. Frame (b) suggests that Galinstan droplets equilibrate to the spherical shape more rapidly, as most of the ligaments rapidly recoil from the elongated shape because of the larger surface tension. More spherical drops also mean that the  $\text{SMD} = 62.7 \mu\text{m}$  is closer to the values derived by projection,  $\text{SMD}_{\text{top}} = 75.8 \mu\text{m}$ , and  $\text{SMD}_{\text{side}} = 77.8 \mu\text{m}$ .

In reality, the amorphous oxide layer thickness (on the order of  $5\text{--}20 \text{\AA}$ <sup>9</sup>) of Galinstan prevents the bags from achieving very thin walls before breakup and therefore limits the minimum size of the droplets that can be formed. Moreover, while the droplets formed in the simulation tend to rapidly equilibrate to a spherical shape, the Galinstan fragments visualized in the experiment display sharp edges and can be expected to follow a modified size distribution.

### G. Comparison with DIH data for water

The following analysis is limited to the water column since DIH data for Galinstan are not available at the moment. An example of numerically refocused digital in-line hologram of the water droplets was displayed in Fig. 3. Two sets of these measurements were collected 25 mm downstream of the column, of initial diameter  $d_0 = 0.94$ : a temporally resolved  $2\times$  magnification set for droplet tracking with a minimum detectable droplet diameter of  $40 \mu\text{m}$  and a spatially resolved  $6\times$  magnification set for size analysis with a minimum detectable droplet diameter of  $12 \mu\text{m}$ . Data is available at distinct times after the passage of the shock; here, we consider  $\tau \sim 2$  and  $\tau \sim 4$ .

The postprocessing procedure described in Sec. III F is applied here to all the droplets that are found in the computational domain. The choice of drawing statistics from all of the droplets is convenient to quickly collect an adequate sample size, but it is not equivalent to the experimental one; analysis will be replaced in the future by a fixed-plane collection. With the minimum grid size of  $2.6 \mu\text{m}$ , the smallest resolved droplet size is expected to be comparable to the

experiment's at approximately  $10 \mu\text{m}$ . At time  $\tau \sim 2$ , with 1530 samples from DIH, the Sauter mean diameter calculated with Eq. (21) is  $\text{SMD}_{\text{exp}} = 59.9 \mu\text{m}$ . With 490 samples from the simulation,  $\text{SMD} = 49.4 \mu\text{m}$  with Eq. (17); the value of the projected SMD [Eq. (21)] varies from  $63.5 \mu\text{m}$  to  $78 \mu\text{m}$  depending on the projection direction. The size distribution comparison between the  $6\times$  DIH data set and the simulation is shown in the normalized histograms of Fig. 18. We see that many of the measured diameters in frame (a) for  $\tau \sim 2$  fall in the  $10$  and  $20 \mu\text{m}$  bins (yellow bars), but that the simulation (blue bars) is not capable of fully capturing that part of the distribution.

At time  $\tau \sim 4$ , additional larger droplets, between  $40$  and  $60 \mu\text{m}$  of volume-equivalent diameter, begin to form because larger portions of the membrane are stripped away by the cross-flow. The DIH measurements (29 915 samples) produce  $\text{SMD}_{\text{exp}} = 109 \mu\text{m}$ , and the simulation (2442 samples) produces  $\text{SMD} = 97.4 \mu\text{m}$ ; the projected SMD values between  $109$  and  $111 \mu\text{m}$  are very close to  $\text{SMD}_{\text{exp}}$ . The size distribution comparison is shown in Fig. 18(b). In this case too, we note that the size distribution from simulation is biased toward larger droplets compared to the DIH distribution.

The gas cross-flow component of the droplets' velocity can be combined with the size distribution data to provide the diameter-velocity diagrams of Fig. 19. In the experiment, the droplets' velocity is measured by tracking sequences of consecutive frames of the  $2\times$  DIH data (see Fig. 3); these values are then directly compared with the center-of-mass velocity of all simulated droplets. Overall, the simulation values (blue crosses) are similarly located with respect to the experiment (red circles), with the most visible difference being the  $40 \mu\text{m}$  threshold of the DIH data since smaller particles are not detectable at this magnification. Figure 19(a), corresponding to  $\tau \sim 2$ , shows a few droplets with negative velocity in the X direction; these smaller droplets are caught in the recirculation zone in the wake of the column, while a few larger drops are accelerated above the gas cross-flow velocity. In Fig. 19(b), corresponding to  $\tau \sim 4$ , negative values of velocity in the X direction are absent as the wake region is weakened by the fragmentation of the column, and the average

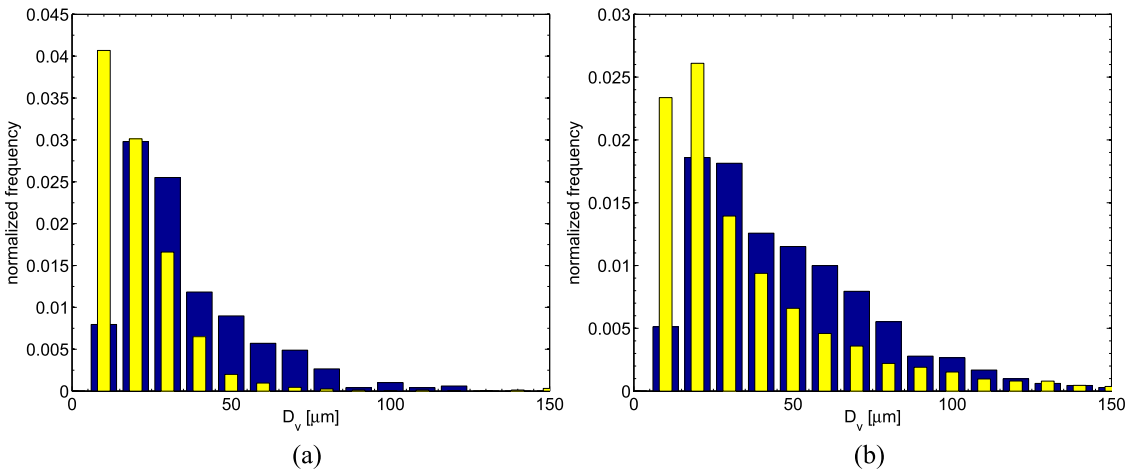


**FIG. 18.** Water droplet size distribution comparison between the  $6\times$  magnification DIH data set (yellow bars) and simulation (blue bars). The plots have all bin width of  $10 \mu\text{m}$ . The normalized histograms are plotted at time  $\tau \sim 2$  (a) with 1530 samples from DIH, 490 samples from simulation, and at time  $\tau \sim 4$  (b) with 29 915 samples from DIH, 2442 samples from simulation.

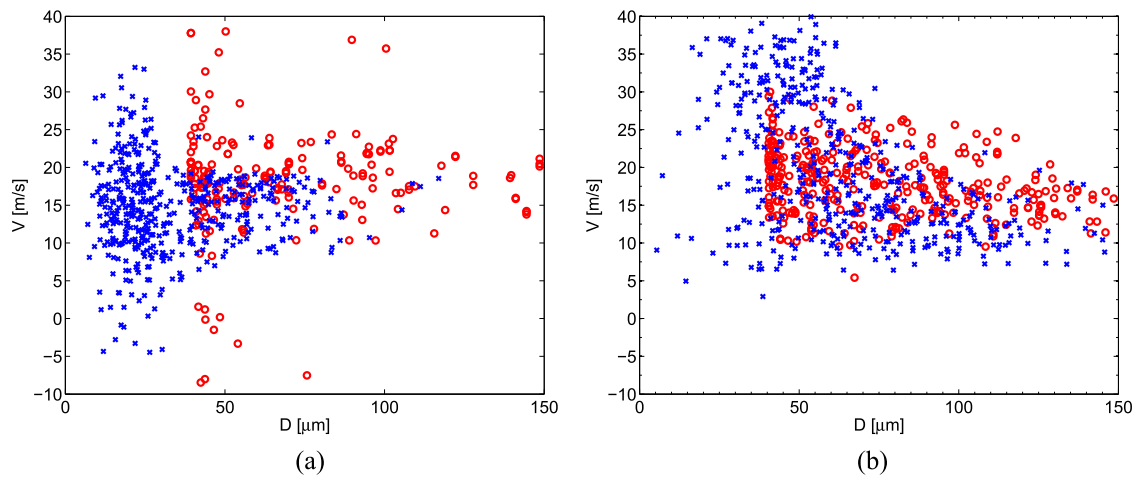


**FIG. 19.** Diameter-velocity diagrams from the 2 $\times$  DIH (red circles) and from simulation (blue crosses) at times  $\tau \sim 2$  in frame (a) and  $\tau \sim 4$  in frame (b). In frame (b), down-sampling was carried out to reduce clutter by a ratio 1:40 for the experiment and 1:2 for the simulation.

velocity has increased but still not reached the gas cross-flow average value.

#### IV. SUMMARY AND CONCLUSIONS

Detailed, time-resolved 3-D simulations of the multimode breakup of aerodynamically loaded liquid columns are presented for two fluids, water and Galinstan, that exhibit substantially different density, viscosity, and surface tension. By complementing the experimental campaign of Chen *et al.*<sup>5</sup> with this numerical study, we report the first direct comparison of simulation data to experimental data allowing for comparison of the shape of the columns, their trajectory, and the spray characteristics. The study is organized to determine whether the morphology of aerodynamic breakup of a liquid metal at moderate Weber numbers can be predicted using the same correlations and models developed for traditional liquids. While our experimental observations show that the time scales over which surface oxide forms are comparable or faster than the experiment's time scale, the simulation suggests that the dynamics of liquid metal can be modeled by the general hydrodynamic framework for two-phase flow up to the moment of membrane burst.

A remarkable similarity in the deformation and cross-flow acceleration of the two columns at similar Weber numbers is observed when the time after the passage of the shock wave is nondimensionalized with the liquid-gas density ratio. This similarity suggests that for the first 2.5 nondimensional times, the acceleration and deformation of liquid metal columns can be predicted by the same correlations as traditional fluids and scale with  $\sqrt{(\rho_G/\rho_L)}$ .

As the liquid column accelerates in the gas cross-stream direction, it presents a concave surface to the incoming airflow and later forms a central stem along the upwind surface. This central stem differentiates the multimode breakup from single-bag breakup and can be explained by extending the linear stability criterion that has been applied to spherical drops under similar accelerating conditions. The criterion is whether the most unstable wavelength of the Rayleigh-Taylor instability is contained more than once within the

column width. Interestingly, the RTI critical wavelength exposes a new dependence on the material properties in the form of  $\sqrt{\sigma/\rho_L}$ . Potentially, different values of  $\sigma/\rho_L$  could lead to different breakup morphologies even with similar Weber numbers. While the critical wavelength increases only by about 20% from water to Galinstan, RTI analysis could explain why the strong similarity of multimode breakup for the two material does not occur at exactly the same Weber numbers:  $We = 12.6$  for water and  $We = 10.2$  for Galinstan. This effect may also be linked with the observation, reported in Ref. 5 and visible in Fig. 1 (Multimedia view), of systematically earlier breakup of Galinstan with respect to water (in nondimensional time) at the same Weber number.

The last part of this study is devoted to the comparison of the spray characteristics with the DIH-derived measurements for water. We note that, while the DIH data are obtained from a single experiment reported in Ref. 5, the current analysis has to contend with the run-to-run variability in bag formation behavior that is discussed in Sec. III B. Shortly after membrane breakup, the particle population is composed of small, deformed droplets that tend to be entrained by the gas cross-flow, with a few droplets recirculating in the column's extended wake. From direct comparison with near-field DIH data, we observe that the 5–15  $\mu\text{m}$  droplet population is not completely captured by the simulation even with an effective grid resolution in 2.6  $\mu\text{m}$ . This gap is indicative of the challenge of numerically resolving the stretching and breakup of a liquid membrane.

Because of the oxidation of the metal's surface, the Galinstan simulation substantially diverges from the experiment in the bag breakup process. Surface oxides resist deformation by absorbing kinetic energy and control the size and shape of the fragments, which appear jagged and irregular. From a physical standpoint, introducing the effects of the metal oxide layer requires tracking the thickness of the layer and mapping it to the rate of change of surface tension. Information of this type is available only for very few materials. New fluid can also replace the existing oxide layer because of internal churning. Computationally, these processes need to be tracked

in time at the metal surface—a capability that is more conveniently provided by a Lagrangian, rather than Eulerian, approach. Thus, in the framework of the computational model presented here, it seems that a hybrid approach where surface capturing is augmented by a Lagrangian component (particles or actual surface mesh) is the most promising path forward.

## ACKNOWLEDGMENTS

This work was supported by the Laboratory Directed Research and Development program at Sandia, which is a multimission laboratory managed and operated by National Technology and Engineering Solutions of Sandia, LLC., a wholly owned subsidiary of Honeywell International, Inc., for the U.S. Department of Energy's National Nuclear Security Administration under Contract No. DE-NA-0003525.

## REFERENCES

- <sup>1</sup>M. Pilch and C. A. Erdman, "Use of breakup time data and velocity history data to predict the maximum size of stable fragments for acceleration-induced breakup of a liquid drop," *Int. J. Multiphase Flow* **13**(6), 741–757 (1987).
- <sup>2</sup>D. Guildenbecher, C. López-Rivera, and P. Sojka, "Secondary atomization," *Exp. Fluids* **46**(3), 371–402 (2009).
- <sup>3</sup>T. G. Theofanous, "Aerobreakup of Newtonian and viscoelastic liquids," *Annu. Rev. Fluid Mech.* **43**(1), 661–690 (2011).
- <sup>4</sup>Y. Chen, E. P. DeMauro, J. L. Wagner, M. Arienti, D. R. Guildenbecher, P. A. Farias, T. W. Grasser, P. D. Sanderson, S. W. Albert, A. M. Turpin, W. Sealy, and R. S. Ketchum, "Aerodynamic breakup and secondary drop formation for a liquid metal column in a shock-induced cross-flow," in *Proceedings of 55th AIAA Aerospace Sciences Meeting* (AIAA, 2017).
- <sup>5</sup>Y. Chen, J. L. Wagner, P. A. Farias, E. P. DeMauro, and D. R. Guildenbecher, "Galinstan liquid metal breakup and droplet formation in a shock-induced cross-flow," *Int. J. Multiphase Flow* **106**, 147–163 (2018).
- <sup>6</sup>S. S. Jain, N. Tyagi, R. S. Prakash, R. V. Ravikrishna, and G. Tomar, "Secondary breakup of drops at moderate Weber numbers: Effect of density ratio and Reynolds number," *Int. J. Multiphase Flow* **117**, 25–41 (2019).
- <sup>7</sup>D. Igra, T. Ogawa, and K. Takayama, "A parametric study of water column deformation resulting from shock wave loading," *Atomization Sprays* **12**(5–6), 577–591 (2002).
- <sup>8</sup>D. Igra and A. Takayama, "Investigation of aerodynamic breakup of a cylindrical water droplet," *Atomization Sprays* **11**(2), 167–185 (2001).
- <sup>9</sup>M. Dickey, "Emerging applications of liquid metals featuring surface oxides," *ACS Appl. Mater. Interfaces* **6**(21), 18369–18379 (2014).
- <sup>10</sup>H. Li, S. Mei, L. Wang, Y. Gao, and J. Liu, "Splashing phenomena of room temperature liquid metal droplet striking on the pool of the same liquid under ambient air environment," *Int. J. Heat Mass Transfer* **47**, 1–8 (2014).
- <sup>11</sup>Y. Chen, D. R. Guildenbecher, K. N. G. Hoffmeister, M. A. Cooper, H. L. Stauffacher, M. S. Oliver, and E. B. Washburn, "Study of aluminum particle combustion in solid propellant plumes using digital in-line holography and imaging pyrometry," *Combust. Flame* **182**, 225–237 (2017).
- <sup>12</sup>X. Zhao, S. Xu, and J. Liu, "Surface tension of liquid metal: Role, mechanism and application," *Front. Energy* **11**(4), 535–567 (2017).
- <sup>13</sup>J.-C. Yang, T.-Y. Qi, T.-Y. Han, J. Zhang, and M.-J. Ni, "Elliptical spreading characteristics of a liquid metal droplet impact on a glass surface under a horizontal magnetic field," *Phys. Fluids* **30**, 012101 (2018).
- <sup>14</sup>M. Gorokhovski and M. Herrmann, "Modeling primary atomization," *Annu. Rev. Fluid Mech.* **40**(1), 343–366 (2008).
- <sup>15</sup>X. Yang and A. Turan, "Simulation of liquid jet atomization coupled with forced perturbation," *Phys. Fluids* **29**(2), 022103 (2017).
- <sup>16</sup>X. Li and M. C. Soteriou, "High fidelity simulation and analysis of liquid jet atomization in a gaseous crossflow at intermediate Weber numbers," *Phys. Fluids* **28**(8), 082101 (2016).
- <sup>17</sup>X. Li, H. Gao, and M. C. Soteriou, "Investigation of the impact of high liquid viscosity on jet atomization in crossflow via high-fidelity simulations," *Phys. Fluids* **29**(8), 082103 (2017).
- <sup>18</sup>S. S. Deshpande, S. R. Gurjar, and M. F. Trujillo, "A computational study of an atomizing liquid sheet," *Phys. Fluids* **27**(8), 082108 (2015).
- <sup>19</sup>A. Zandian, W. A. Sirignano, and F. Hussain, "Planar liquid jet: Early deformation and atomization cascades," *Phys. Fluids* **29**(6), 062109 (2017).
- <sup>20</sup>V. Sanjay and A. K. Das, "Formation of liquid chain by collision of two laminar jets," *Phys. Fluids* **29**(11), 112101 (2017).
- <sup>21</sup>P. Zhang and B. Wang, "Effects of elevated ambient pressure on the disintegration of impinged sheets," *Phys. Fluids* **29**(4), 042102 (2017).
- <sup>22</sup>H. Yang and J. Peng, "Numerical study of the shear-thinning effect on the interaction between a normal shock wave and a cylindrical liquid column," *Phys. Fluids* **31**(4), 043101 (2019).
- <sup>23</sup>C. Shao, K. Luo, Y. Yang, and J. Fan, "Direct numerical simulation of droplet breakup in homogeneous isotropic turbulence: The effect of the Weber number," *Int. J. Multiphase Flow* **107**, 263–274 (2018).
- <sup>24</sup>N. Liu, Z. Wang, M. Sun, H. Wang, and B. Wang, "Numerical simulation of liquid droplet breakup in supersonic flows," *Acta Astronaut.* **145**, 116–130 (2018).
- <sup>25</sup>M. Jalal and K. Mehravar, "Transient growth of droplet instabilities in a stream," *Phys. Fluids* **26**(1), 012101 (2014).
- <sup>26</sup>M. Arienti, X. Li, M. C. Soteriou, C. A. Eckett, M. Sussman, and R. J. Jensen, "Coupled level-set/volume-of-fluid method for simulation of injector atomization," *J. Propul. Power* **29**(1), 147–157 (2012).
- <sup>27</sup>J. L. Wagner, E. P. DeMauro, K. M. Casper, S. J. Beresh, K. P. Lynch, and B. O. Pruitt, "Pulse-burst PIV of an impulsively started cylinder in a shock tube for  $Re > 10^5$ ," *Exp. Fluids* **59**(6), 106 (2018).
- <sup>28</sup>J. Eggers, "Universal pinching of SD axisymmetric free-surface flow," *Phys. Rev. Lett.* **71**, 3458–3460 (1993).
- <sup>29</sup>M. Moseler and U. Landman, "Formation, stability, and breakup of nanojets," *Science* **289**, 1165–1169 (2000).
- <sup>30</sup>M. Herrmann, "On simulating primary atomization using the refined level set grid method," in *Proceedings of Americas 21st Annual Conference on Liquid Atomization and Spray Systems*, 2008.
- <sup>31</sup>M. Jemison, E. Loch, M. Sussman, M. Shashkov, M. Arienti, M. Ohta, and Y. Wang, "A coupled level set-moment of fluid method for incompressible two-phase flows," *J. Sci. Comput.* **54**(2–3), 454–491 (2013).
- <sup>32</sup>M. Jemison, M. Sussman, and M. Arienti, "Compressible, multiphase semi-implicit method with moment of fluid interface representation," *J. Comput. Phys.* **279**, 182–217 (2014).
- <sup>33</sup>M. Arienti and M. Sussman, "A Numerical study of the thermal transient in high-pressure diesel injection," *Int. J. Multiphase Flow* **88**, 205–221 (2017).
- <sup>34</sup>M. Sussman, K. M. Smith, M. Y. Hussaini, M. Ohta, and R. Zhi-Wei, "A sharp interface method for incompressible two-phase flows," *J. Comput. Phys.* **221**, 469–505 (2007).
- <sup>35</sup>E. Aulisa, S. Manservisi, R. Scardovelli, and S. Zaleski, "Interface reconstruction with least-squares fit and split advection in three-dimensional Cartesian geometry," *J. Comput. Phys.* **225**(2), 2301–2319 (2007).
- <sup>36</sup>M. Arienti and M. Sussman, "An embedded level set method for sharp-interface multiphase simulations of diesel injectors," *Int. J. Multiphase Flow* **59**, 1–14 (2014).
- <sup>37</sup>M. Sussman and M. Ohta, "A stable and efficient method for treating surface tension," *SIAM J. Sci. Comput.* **31**, 2447–2471 (2009).
- <sup>38</sup>A. T. Philip, *Compressible Fluid Dynamics* (McGraw-Hill, Inc., USA, 1972).
- <sup>39</sup>T. Liu, P. Sen, and C.-J. Kim, "Characterization of liquid-metal Galinstan® for droplet applications," in *2010 IEEE 23rd International Conference on Micro Electro Mechanical Systems (MEMS)* (IEEE, 2010).
- <sup>40</sup>H. J. Holterman, *Kinetics and Evaporation of Water Drops in Air* (Wageningen, IMAG, 2003), Vol. 2012.
- <sup>41</sup>MATLAB and Statistics Toolbox Release 2014b, The MathWorks, Inc., Natick, Massachusetts, USA, 2014.
- <sup>42</sup>Y. A. Cengel and J. M. Cimbala, *Fluid Mechanics: Fundamentals and Applications*, 2nd ed. (McGraw-Hill, 2010).
- <sup>43</sup>M. Arienti, Y. Chen, J. Wagner, and D. Guildenbecher, "Aerodynamic breakup of liquid metal in a shock-induced crossflow," in *Proceedings of*

Americas 29th Annual Conference on Liquid Atomization and Spray Systems, 2017.

<sup>44</sup>H. Zhao, H.-F. Liu, W.-F. Li, and J.-L. Xu, "Morphological classification of low viscosity drop bag breakup in a continuous air jet stream," *Phys. Fluids* **22**, 114103 (2010).

<sup>45</sup>H. Zhao, H.-F. Liu, J.-L. Xu, W.-F. Li, and K.-F. Lin, "Temporal properties of secondary drop breakup in the bag-stamen breakup regime," *Phys. Fluids* **25**, 054102 (2013).

<sup>46</sup>S. Chandrasekhar, *Hydrodynamic and Hydromagnetic Stability*, International Series of Monographs on Physics (Clarendon, Oxford, 1961).